

Intensity-Spatial Dual Masked Autoencoder for Multi-Scale Feature Learning in Chest CT Segmentation

1st Yuexing Ding
ZJU ARClab
Zhejiang University
Hangzhou, China
22221177@zju.edu.cn

2nd Jun Wang
school of computer and computing science
Hangzhou City University
Hangzhou, China
wjcy19870122@163.com

3rd Hongbing Lyu
ZJU ARClab
Zhejiang University
Hangzhou, China
lhb@zju.edu.cn

Abstract—In the field of medical image segmentation, challenges such as indistinct lesion features, ambiguous boundaries, and multi-scale characteristics have long prevailed. This paper proposes an improved method named Intensity-Spatial Dual Masked AutoEncoder (ISD-MAE). Based on the tissue-contrast semi-masked autoencoder, a Masked AutoEncoder (MAE) branch is introduced to perform intensity masking and spatial masking operations on chest CT images for multi-scale feature learning and segmentation tasks. The model utilizes a dual-branch structure and contrastive learning to enhance the ability to learn tissue features and boundary details. Experiments are conducted on multiple 2D and 3D datasets. The results show that ISD-MAE significantly outperforms other methods in 2D pneumonia and mediastinal tumor segmentation tasks. For example, the Dice score reaches $90.10 \pm 0.54\%$ on the COVID19_LESION dataset, and the performance is relatively stable. However, there is still room for improvement on 3D datasets. In response to this, improvement directions are proposed, including optimizing the loss function, using enhanced 3D convolution blocks, and processing datasets from multiple perspectives. Our code is available at: <https://github.com/prowontheus/ISD-MAE>

Index Terms—Self-supervised Learning, Masked Image Modeling, Autoencoder, U-Net

I. INTRODUCTION

Medical images often exhibit complex structures and features. Self-supervised pretraining models can learn universal image features, such as texture, shape, and edges, from a large amount of unlabeled medical image data. These universal features are crucial for subsequent medical image segmentation tasks, providing the model with richer information. However, medical image processing faces various challenges, such as ambiguous lesion features, unclear boundaries, and multiscale features, which have long plagued researchers. To effectively overcome these challenges, researchers have been exploring various methods and techniques, with masking strategies gradually gaining attention as an important pretraining approach.

Among the many self-supervised learning methods, Masked Image Modeling (MIM) [2] [3] is becoming increasingly popular. By randomly masking parts of the image content and tasking the model to predict the masked portions based on the visible parts, the model can capture the correlations and dependencies

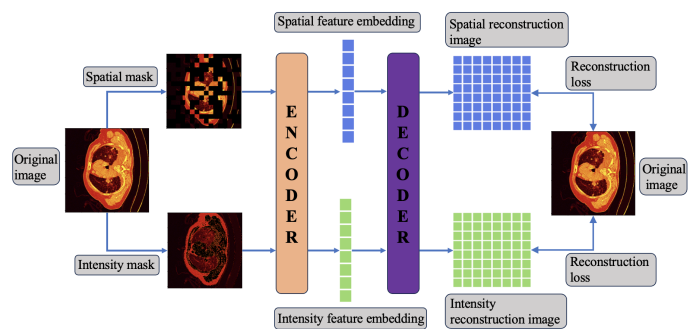


Fig. 1: An Overview of our ISD-MAE structure. First, the input image is fed into two branches. In the first branch, patches are randomly masked according to preset ratios and patch sizes to create a Spatial mask. In the other branch, grayscale values of the image are also randomly masked at preset ratios to create an intensity mask. Subsequently, these two corrupted images are input into the encoder to obtain feature embeddings for each branch. They are then separately fed into the decoder to reconstruct images for each branch. Finally, losses are calculated separately with the original image for each branch.

between different regions in the image, thus gaining a more comprehensive understanding of the image’s semantic information. In MIM, the model needs to learn both low-level features of the image (such as color, texture, etc.) and high-level semantic information (such as object categories, scene understanding, etc.). However, during training, the model may overly focus on reconstructing the masked pixel values and overlook learning the high-level semantic information. This could lead to poor performance of the model in downstream tasks, as these tasks rely more on the model’s understanding of the high-level semantics of the image.

Therefore, Huang et al. proposed Contrastive Masked AutoEncoder (CMAE) [1]. Building upon the foundation of masked image modeling, CMAE incorporates contrastive learning. It consists of two branches: an online branch for reconstructing masked images and a target branch that receives complete image inputs through momentum-updated encoders. Subsequently, the features from the online branch and the target branch are compared, enabling the model to learn

not only how to reconstruct images but also the differences between different images, enhancing feature distinctiveness and robustness.

In medical imaging, CT images are composed of the different Hounsfield Unit (HU) spectra, and HU values can help distinguish various human tissues. By observing HU values, it is possible to assist in determining the type of tissue present in the image, which is crucial for medical diagnosis, especially in detecting conditions such as tumors and cysts, where the HU values of the diseased tissue may differ from the surrounding normal tissue. To address this, Zheng et al. proposed the Tissue-Contrast Semi-Masked AutoEncoder (TCS-MAE) [4]. This method utilizes a density-based masking strategy, randomly masking HU values at evenly spaced intervals based on the different characteristic ranges of HU spectra occupied by various tissues, and then reconstructing the masked tissue regions during training to enable the model to more effectively capture feature representations of different tissues.

However, we have also found that spatial masking strategies have their unique advantages. Spatial masking divides the image into multiple small patches for masking, allowing the model to focus more on the local structure and detailed information of the image. For instance, in lung CT images, features such as small nodules and textures in the lungs are more easily learned and understood at the spatial level, while randomly masking HU values may potentially disrupt the integrity of this local structural information to some extent. Therefore, building upon the work of Zheng et al., we propose a novel pretraining method for chest CT images called Intensity-Spatial Dual Masked AutoEncoder (ISD-MAE). Based on TCS-MAE [4], we introduce a second branch - the Masked AutoEncoder (MAE) [3] - and perform contrastive learning reconstruction of images through both branches to optimize the performance of medical image classification and segmentation tasks. A simple overview is shown in Fig. 1.

We conducted experiments on three downstream tasks, including pneumonia detection, pneumonia segmentation, and mediastinal region segmentation. The experimental results indicate that our ISD-MAE method can more effectively learn tissue structure representations and significantly improve the classification and segmentation performance of downstream tasks compared to existing pretraining methods.

II. RELATED WORK

A. U-Net Architecture

The U-Net architecture, proposed by Ronneberger et al. [5], is a classic structure in the field of medical image analysis. This architecture consists of symmetric encoders and decoders. The encoder gradually reduces the spatial resolution of input images through a series of convolutional and pooling layers (downsampling layers), capturing high-level features such as edges, textures, and shapes. The decoder, on the other hand, restores the spatial resolution of the image through a series of transpose convolutional layers (upsampling layers) and convolutional layers. At each layer, the decoder concatenates feature maps from the corresponding encoder layer, allowing

the transfer of low-level detail information to higher-level feature maps, ultimately reconstructing the feature maps to pixel-level predictions.

3D U-Net [6] is an extended version based on the U-Net architecture, specifically designed for handling three-dimensional data in medical images. In comparison to the U-Net, 3D U-Net utilizes three-dimensional convolution operations. Taking into account the global information of 3D data, it reduces the number of downsampling steps to avoid excessive loss of spatial information and decreases the network's parameter count.

Zhou et al. [7] introduced a nested U-Net architecture called U-Net++. This architecture nests the encoders and decoders of U-Net at multiple levels, with each level having its own encoder and decoder. Through cross-layer connections for information transfer, the network can better capture multi-scale information. Additionally, a dense connection mechanism is introduced, allowing each decoder layer to access information from all preceding encoder layers, enhancing feature propagation and utilization.

B. Autoencoder

The architecture of autoencoders originates from the fields of neural networks and unsupervised learning. Initially proposed by Hinton et al. [8] as stacked denoising autoencoders, the core idea is to reconstruct input data by learning compressed representations of the data, thereby achieving dimensionality reduction. Subsequently, Vincent et al. [9] introduced a variant of autoencoders called "Denoising Autoencoder," aimed at learning robust feature representations of data. Unlike traditional autoencoders, denoising autoencoders are trained by introducing noise (such as additive Gaussian noise) into the input data to learn feature representations robust to noise.

Kingma et al. [10] combined autoencoders with probabilistic generative models and introduced a novel generative model known as the Variational Autoencoder (VAE), incorporating variational inference methods. This approach trains the autoencoder by maximizing the Evidence Lower Bound (ELBO) to learn the latent distribution of data, enabling the generation of new data samples. This method provides an innovative approach for exploring the latent structure of data and generating new data samples.

C. Contrastive Learning

Contrastive Learning (CL) is a self-supervised learning method used for learning data representations, with the core idea of comparing the similarities and differences between different samples. Chen et al. [11] introduced the SimCLR framework for contrastive learning of visual representations. This model aims to maximize the similarity of positive sample pairs and minimize the similarity of negative sample pairs to learn visual representations. SimCLR employs robust data augmentation strategies and contrastive loss functions, enabling the model to learn visually rich representations with semantic information from large-scale unlabeled image data.

Moco [12] proposed by He et al. explores the path of learning visual representations through contrastive learning in the absence of label information. This method leverages the idea of momentum contrast, introducing momentum updates during training to establish similarity relationships between positive and negative sample pairs.

Grill et al. [13] explored the novel method of BYOL for contrastive self-supervised learning, training the model solely on different views of the same image (positive sample pairs) to learn similar representations of the same image from different perspectives, achieving self-supervised learning. This method does not require learning from negative sample pairs, distinguishing it significantly from traditional contrastive learning methods [11] [2].

Caron et al. [14] introduced the new features presented by self-supervised learning on the Vision Transformer (ViT) and proposed a concise and effective self-supervised learning method called self-distillation with no labels (DINO). This method combines techniques such as momentum encoders, multi-crop training, and small patches to learn useful image representations through knowledge distillation between student and teacher networks.

Inspired by the aforementioned studies, some researchers have begun to apply contrastive learning and autoencoders to medical image research. For instance, Chaitanya et al. [15] introduced contrastive learning into the field of medical image segmentation for the first time, proposing a local contrastive loss to enhance the latent representations generated by the encoder, effectively alleviating the issue of insufficient annotated datasets in medical image analysis. Chen et al. [16] introduced Convolutional Autoencoder for Nodule Classification (CANN) for lung nodules. They successfully extracted accurate image features with only a small amount of data, enabling faster labeling of medical data.

Additionally, CMAE [1] and TCS-MAE [4] also integrated contrastive learning and masked image modeling. However, these studies either focused solely on spatial-level masking methods or only considered the tissue distribution in medical images, without integrating both aspects comprehensively.

III. METHODS

A. Image Preprocessing

a) 2D images: Firstly, we resize the original image to change the image dimensions from (3, H, W) to (3, 256, 256). We then perform window width and level adjustment. The window width controls the grayscale range displayed, which affects the contrast of the display. A larger window width stretches the grayscale range displayed, making image details clearer and more visible. The window level sets the center grayscale value displayed, adjusting the window level can change the brightness of the image. Typically, 2D lung CT images have only one channel. Therefore, we combine the original lung image, mediastinal image, and edge image into three channels of an RGB image as input for the 2D image.

The lung images and mediastinal images are derived from original 2D chest CT images through window width and level

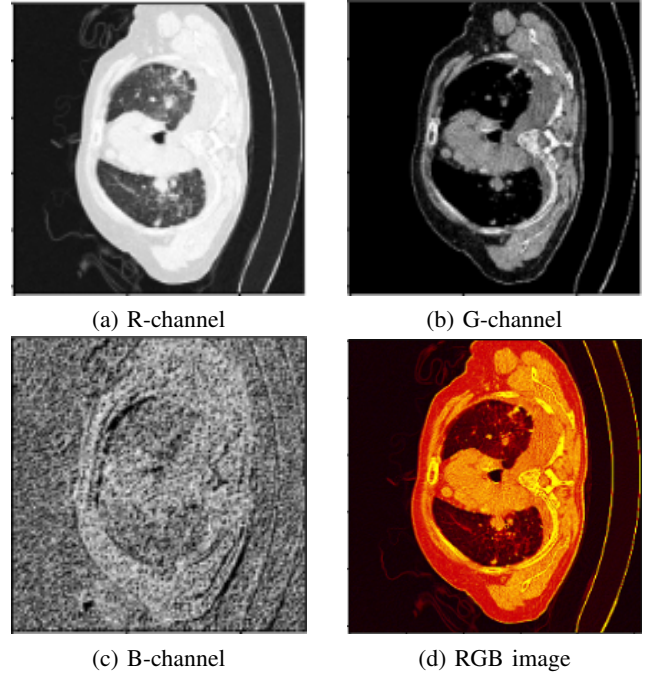


Fig. 2: Displays the effects of the synthesis of the three channels and the RGB image using the method we have described. These three channels contain better contrast and richer edge information from the original image.

adjustments, while the edge image is obtained by sharpening with the Sobel operator, which can highlight the contours of tissue structures, aiding the model in better understanding the internal structures and boundaries of the image. The composition of the input RGB image is as follows:

$$\mathbf{I} = (\mathbf{I}_{lung}, \mathbf{I}_{medi}, \mathbf{I}_{edge}) \quad (1)$$

where

$$\mathbf{I}_{lung} = \left(\frac{I_{ct} - L_{lung} + 0.5 * W_{lung}}{W_{lung}} \right) * 255 \quad (2)$$

$$\mathbf{I}_{medi} = \left(\frac{I_{ct} - L_{medi} + 0.5 * W_{medi}}{W_{medi}} \right) * 255 \quad (3)$$

Here, I_{ct} represents the original image, where $L_{lung} = -500$ HU, $W_{lung} = 1200$ HU, $L_{medi} = 30$ HU, and $W_{medi} = 300$ HU. Setting these values can make the tissue structures, tumors, inflammations, and other lesion areas in the lungs clearer.

\mathbf{I}_{edge} is obtained by applying the Sobel operator to the combination of \mathbf{I}_{lung} and \mathbf{I}_{medi} . The Sobel operator consists of a horizontal convolution kernel G_x and a vertical convolution kernel G_y :

$$\mathbf{S}_x = G_x * \mathbf{I}_*, \mathbf{S}_y = G_y * \mathbf{I}_* \quad (4)$$

Here, \mathbf{I}_* denotes \mathbf{I}_{lung} or \mathbf{I}_{medi} . G_x and G_y represent the Sobel operator, as follows:

$$G_x = \begin{bmatrix} -1 & 0 & 1 \\ -2 & 0 & 2 \\ -1 & 0 & 1 \end{bmatrix}, G_y = \begin{bmatrix} -1 & -2 & -1 \\ 0 & 0 & 0 \\ 1 & 2 & 1 \end{bmatrix} \quad (5)$$

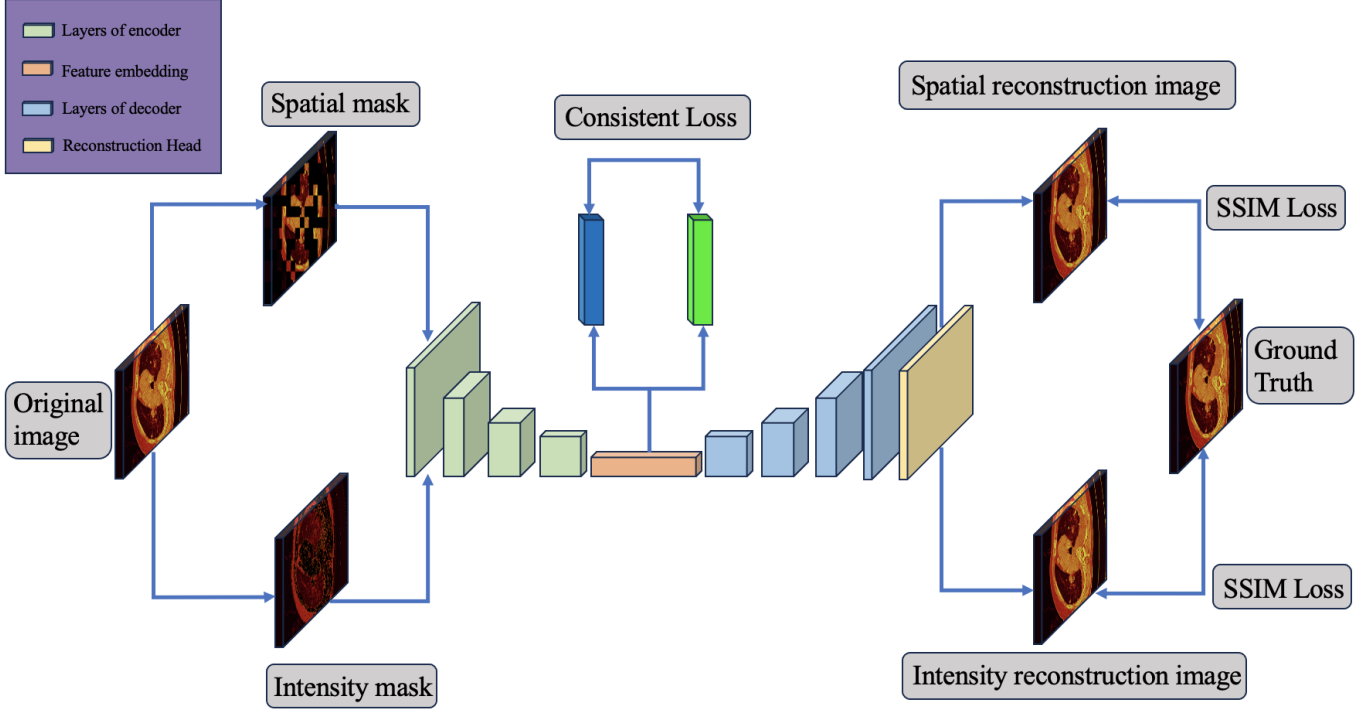


Fig. 3: Intensity-Spatial Dual Masked Autoencoder

Then, obtain the edge images of the lung and mediastinum through the following calculations respectively:

$$\mathbf{I}_{edge}^* = \sqrt{\mathbf{S}_x^2 + \mathbf{S}_y^2} \quad (6)$$

where \mathbf{I}_{edge}^* denotes \mathbf{I}_{edge}^{lung} and \mathbf{I}_{edge}^{medi} . Finally, we combine the obtained edge images of the lung and mediastinum to obtain the final edge image:

$$\mathbf{I}_{edge} = \max\{\mathbf{I}_{edge}^{lung}, \mathbf{I}_{edge}^{medi}\} \quad (7)$$

By taking the maximum value of two images processed with the Sobel operator, not only can noise interference be reduced, but it also provides the network with more information and contrast. Fig. 2 shows the effect of the synthesis of the three channels using the above method.

b) 3D images: Similar to the preprocessing method for 2D images, 3D chest CT images also need to be adjusted from dimensions $(1, H, W, D)$ to $(1, 256, 256, 256)$. We adjust the thickness between layers in the H, W, and D directions using interpolation to a uniform thickness of 1mm. This helps reduce differences between images with varying layer thicknesses. Uniformly thick images typically exhibit a smoother and more continuous appearance, enhancing visual quality and leading to clearer and more accurate segmentation results. We then proceed to slice the 3D images layer by layer in the D dimension. Following this, we construct RGB channels for each image layer by layer. Ultimately, our preprocessed images expand from a $(1, 256, 256, 256)$ dimension to $(3, 256, 256, 256)$.

B. Generating mask images

a) Intensity mask: Assuming the input chest CT image is denoted as \mathbf{I} , The method for generating an intensity mask on a Chest CT image can be described as follows:

- Normalize the pixel values of the chest CT image \mathbf{I} to the range $[0, 1]$:

$$\mathbf{I}_n = \frac{\mathbf{I} - \min(\mathbf{I})}{\max(\mathbf{I}) - \min(\mathbf{I})} \quad (8)$$

- Convert the normalized image \mathbf{I}_n to a grayscale image \mathbf{I}_g using The luminosity method.

$$\mathbf{I}_g = 0.2989 * \mathbf{I}_n^r + 0.5870 * \mathbf{I}_n^g + 0.1140 * \mathbf{I}_n^b \quad (9)$$

Where, \mathbf{I}_n^r , \mathbf{I}_n^g , and \mathbf{I}_n^b represent the red, green, and blue channel slices of image \mathbf{I}_n , respectively.

- Divide the interval $[0, 1]$ into K equal partitions, which form the set of \mathbf{S} . Here, K is a hyperparameter predetermined regarding the mask scale. Subsequently, based on the intensity mask ratio parameter $r_t \in (0, 1)$, randomly select $K \cdot r_t$ intervals from \mathbf{S} to compose the set \mathbf{S}_m .

$$\mathbf{S} = \{[\frac{i}{K}, \frac{i+1}{K}] | i = 0, 1, \dots, K-1\} \quad (10)$$

$$\mathbf{S}_m = \binom{|\mathbf{S}|}{K \cdot r_t} \quad (11)$$

- For each pixel $\mathbf{G}_{i,j}$ in the grayscale image \mathbf{I}_g , if it falls within any of the set \mathbf{S}_m , set the RGB values at the

corresponding position (i, j) in the original image \mathbf{I} to zero:

$$\mathbf{I}_{i,j} = \begin{cases} [0, 0, 0] & \text{if } \mathbf{G}_{i,j} \text{ falls in any of } \mathcal{S}_m, \\ \mathbf{I}_{i,j} & \text{otherwise} \end{cases} \quad (12)$$

Ultimately, $\mathbf{I}_{i,j}$ forms the image of the intensity mask image \mathbf{I}_m^t .

b) *Spatial mask*: The method of spatial masking is consistent with the MAE [3]. First, set hyperparameters \mathbf{P} and r_t , representing spatial mask size and mask ratio, respectively. Divide the image into grids of size \mathbf{P} , then select a certain number of patches based on ratio r_t and set the pixel values in these patches to 0. In the end, we obtain the image with spatial masking, denoted as \mathbf{I}_m^p .

C. Encoder and decoder

Fig. 3 illustrates our ISD-MAE framework. Overall, the entire network follows the U-Net [5] architecture, but with slight differences. Firstly, we replaced the encoder part with SegFormer, proposed by Xie et al. [17] SegFormer is an efficient semantic segmentation framework that combines Transformers with lightweight multilayer perceptron (MLP) decoders. It does not require positional encoding and integrates local and global attention, enabling the efficient output of multiscale features. These characteristics make SegFormer superior to traditional U-Net encoders in feature extraction.

The original image is preprocessed using the methods introduced in III-A and III-B to obtain intensity mask images and spatial mask images, respectively. Then, they are subjected to random horizontal and vertical flips, arbitrary angle rotations, and scaling with a certain probability to enhance the model’s robustness and reduce overfitting.

Then, they are input into the encoder separately. After 5 rounds of downsampling, the size of the feature maps gradually decreases while the number of channels increases. The final layer’s feature map has 512 channels, with an image size of $8 * 8$ (for 3D images, the size is $8 * 8 * 8$). Next, the feature map from the last layer is fed into the decoder, and nearest-neighbor interpolation is used for upsampling. The upsampled feature map is then concatenated with the corresponding feature map from the encoder’s layer. After 5 rounds of such upsampling operations, the feature map size gradually recovers, and the number of channels decreases to 128, forming a decoder output of dimensions (128, 256, 256). Finally, after passing through a reconstruction head module, it is restored to the original image size of (3, 256, 256). This process results in the reconstructed image.

D. Loss function

a) *SSIM loss*: The first part is the similarity loss between the output of the decoder and the ground truth image, which utilizes the Structural Similarity Index Measure (SSIM) loss function [18].

For two images \mathbf{I} and \mathbf{I}_m^* , the calculation formula of SSIM is as follows:

$$SSIM(\mathbf{I}, \mathbf{I}_{out}^*) = \frac{(2\mu_g\mu_o + C_1)(2\mu_{go} + C_2)}{(\mu_g^2 + \mu_o^2 + C_1)(\sigma_g^2 + \sigma_o^2 + C_2)} \quad (13)$$

\mathbf{I}_{out}^* represents \mathbf{I}_{out}^t and \mathbf{I}_{out}^p . They are the output results of the intensity masked image and the spatial masked image passing through the model respectively. μ_g and μ_o are the means of images \mathbf{I} and \mathbf{I}_{out}^* , σ_g and σ_o are their standard deviations, μ_{go} is the covariance of \mathbf{I} and \mathbf{I}_{out}^* . C_1 and C_2 are constants used for stability.

The objective function of the model is:

$$\mathcal{L}_{ssim} = \overline{[1 - SSIM(\mathbf{I}, \mathbf{I}_m^t)]} + \overline{[1 - SSIM(\mathbf{I}, \mathbf{I}_m^p)]} \quad (14)$$

b) *Contrastive loss*: The second part of the loss function consists of the contrastive loss. The output feature map of the encoder goes through a project head module, which performs average pooling on the feature map, flattens it, and then passes it through a linear layer to obtain a 128-dimensional feature embedding. \mathbf{F}_t represents the embedding of the intensity mask image, and \mathbf{F}_p represents the embedding of the spatial mask image. Then we calculate the contrastive loss:

- Normalize each vector \mathbf{F}_t and \mathbf{F}_p by their \mathcal{L}_2 norms, and calculate the similarity score matrix for the two vectors:

$$\hat{\mathbf{F}}_t = \frac{\mathbf{F}_t}{\|\mathbf{F}_t\|_2}, \hat{\mathbf{F}}_p = \frac{\mathbf{F}_p}{\|\mathbf{F}_p\|_2} \quad (15)$$

$$\hat{\mathbf{S}} = \text{logit_scale} \cdot (\hat{\mathbf{F}}_t \cdot \hat{\mathbf{F}}_p^\top) \quad (16)$$

logit_scale is a constant used to scale the similarity score matrix of embedding vectors, typically set to $\ln(\frac{1}{0.07})$.

- Define the number of classes as *classes*, create class labels *labels* = $[0, 1, \dots, \text{classes} - 1]$, and calculate the cross-entropy loss twice. The final contrastive loss \mathcal{L}_{cons} is the average of the two cross-entropy losses.

$$\mathcal{L}_1 = \text{cross_entropy}(\hat{\mathbf{S}}, \text{labels}) \quad (17)$$

$$\mathcal{L}_2 = \text{cross_entropy}(\hat{\mathbf{S}}^\top, \text{labels})$$

$$\mathcal{L}_{cons} = \frac{1}{2} \cdot (\mathcal{L}_1 + \mathcal{L}_2) \quad (18)$$

The loss function \mathcal{L}_{total} is the sum of the SSIM loss \mathcal{L}_{ssim} and the contrastive loss \mathcal{L}_{cons} :

$$\mathcal{L}_{total} = \mathcal{L}_{ssim} + \mathcal{L}_{cons} \quad (19)$$

E. Datasets

To validate our approach, we first conducted a pre-training task on the TotalSegmentator [19] lung CT scans, and then downstream segmentation and classification tasks were performed on eight 2D datasets and two 3D datasets, as shown in Table I. Among these datasets, GRAM, COVID19_3D, and COVID19_2D are private datasets. These scans are derived from lung CT scans from multiple hospitals. The GRAM dataset consists of 2D images obtained by slicing the 3D lung CT dataset, comprising 4,163 slices with a thickness of 1mm. The COVID19_3D dataset contains 1,238 images, while the COVID19_2D dataset is derived from COVID19_3D through slicing.

TABLE I: The datasets used for validating the experiment.

Datasets	Shape	Samples	Train/Test	Annotation Regions	Epochs	Task
TotalSegmentator [19]	2D/3D	1227/8805	-	Without annotated regions	50	Pretraining
COVID19_LESION	2D	2729	4:1	pneumonia	30	Segmentation
Task06_Lung	2D	463	4:1	Lung cancer	100	Segmentation
COVID19_2D	2D	1655	4:1	pneumonia	40	Segmentation
Lung_nodule_seg	2D	1657	4:1	Lung nodule	50	Segmentation
Lung_CT_nodule	2D	920	4:1	Lung nodule	40	Segmentation
LIDC_IDRI	2D	1560	4:1	Lung nodule	40	Segmentation
CT Scans for COVID19	2D	13980	4:1	pneumonia	20	Classification
GRAM	2D	4163	4:1	Bacterial infections	50	Classification
COVID19_CT	3D	20	4:1	pneumonia	30	Segmentation
COVID19_3D	3D	1238	4:1	pneumonia	20	Segmentation

F. Details

a) *Pretraining*: We performed pretraining tasks on the chest 3D CT scans and their 2D slices of TotalSegmentator respectively. We ran 50 epochs on NVIDIA RTX 4070 ti super. The learning rate scheduler is StepLR. The step size is 100000 with one batch as one step. The decay rate is set to 0.96. The optimizer used is AdamW. The size of the intensity masking mask and the spatial masking mask are both 16.

b) *Fine-tuning*: In downstream segmentation and classification tasks, we employed the StepLR learning rate scheduler with a step size of 1, invoking the step method once per training epoch, and a decay rate of 0.9. We utilized the AdamW optimizer and employed binary cross-entropy loss as the loss function. The ratio of training to testing sets across all datasets was set to approximately 4:1. Due to GPU memory constraints, the batch size was set to 16 for fine-tuning the 2D models and 1 for the 3D models. Additionally, we adopted mixed precision training, where model weights were stored in float32 during training, gradients were computed in float16, then converted back to single-precision floating point for parameter updates using the optimizer.

G. Metrics

We use Dice Similarity Coefficient(DSC) and Hausdorff distance (HD) to evaluate the performance of our pre-trained model on downstream segmentation tasks and ROC-AUC for evaluating classification tasks.

- The Dice coefficient (DSC) is a metric used to assess the accuracy of image segmentation, commonly employed in the field of medical image segmentation. It measures the similarity of segmentation by calculating the ratio of the overlap between two segmented regions to their total volumes. The formula for the Dice coefficient is as follows:

$$DSC(\mathbf{I}_{out}, \mathbf{I}_g) = \frac{2 \times |\mathbf{I}_{out} \cap \mathbf{I}_g|}{|\mathbf{I}_{out}| + |\mathbf{I}_g|} \quad (20)$$

Where \mathbf{I}_{out} represents the region of the model's segmented result and \mathbf{I}_g represents the region of the ground truth segmentation.

- The Hausdorff distance is a measure describing the distance between two sets of points and is commonly used in fields such as image processing and computer vision to quantify the dissimilarity between two shapes or contours. The Hausdorff distance $H(\mathbf{I}_{out}, \mathbf{I}_g)$ is defined as:

$$\begin{aligned} H(\mathbf{I}_{out}, \mathbf{I}_g) &= \max(h(\mathbf{I}_{out}, \mathbf{I}_g), h(\mathbf{I}_g, \mathbf{I}_{out})) \\ h(\mathbf{I}_{out}, \mathbf{I}_g) &= \max_{a \in \mathbf{I}_{out}} \min_{b \in \mathbf{I}_g} \|a - b\| \\ h(\mathbf{I}_g, \mathbf{I}_{out}) &= \max_{b \in \mathbf{I}_g} \min_{a \in \mathbf{I}_{out}} \|b - a\| \end{aligned} \quad (21)$$

where $(\|\cdot\|)$ represents a distance metric between two points, typically the Euclidean distance.

IV. EXPERIMENTS

In Table II, we present a comparison of the downstream segmentation results on a series of chest CT datasets using our ISD-MAE and numerous state-of-the-art self-supervised learning models. The data in the table represents the segmentation Dice scores of different models on various datasets. The models compared include AE [20], DAE [21], MAE [3], CMAE [1], CAE [22], and MaskFeat [23].

A. Comparison to state of the art methods

From the segmentation results in Table II, it can be seen that ISD-MAE's Dice scores are generally higher than those of other methods across all pneumonia segmentation datasets (COVID19_LESION, COVID19_2D, COVID19_CT, COVID19_3D), especially in the COVID19_LESION dataset, where its Dice score reaches as high as $90.10 \pm 0.54\%$, significantly exceeding the scores of other methods, and the Hausdorff distance values are comparatively lower as well. In the mediastinal tumor datasets (Task06_Lung,

TABLE II: Results of downstream segmentation tasks using different self-supervised methods. In each cell of the table, the number above represents the Dice similarity coefficient (%), while the number below represents the Hausdorff distance (HD). The best score in each row is shown in bold.

Methods \ Datasets	AE	DAE	MAE	CMAE	CAE	MaskFeat	ISD-MAE
COVID19_LESION	85.87 ± 0.88	87.01 ± 0.59	87.72 ± 0.63	88.64 ± 1.03	86.13 ± 0.98	82.22 ± 0.43	90.10 ± 0.54
	14.43 ± 0.13	14.01 ± 0.12	13.72 ± 0.12	13.23 ± 0.11	14.13 ± 0.12	15.28 ± 0.14	12.50 ± 0.10
Task06_Lung	84.70 ± 0.59	86.80 ± 0.48	87.45 ± 0.75	88.23 ± 0.78	86.30 ± 0.60	82.73 ± 0.87	90.02 ± 0.47
	7.87 ± 0.11	7.41 ± 0.09	7.32 ± 0.08	7.04 ± 0.09	7.53 ± 0.09	8.22 ± 0.10	6.44 ± 0.08
COVID19_2D	82.28 ± 1.12	85.78 ± 0.96	85.93 ± 0.89	85.12 ± 1.41	83.34 ± 1.27	85.60 ± 0.43	84.18 ± 0.66
	24.87 ± 0.38	23.01 ± 0.39	22.72 ± 0.44	22.64 ± 0.36	24.13 ± 0.43	25.22 ± 0.40	21.96 ± 0.38
Lung_nodule_seg	85.93 ± 1.96	86.43 ± 1.65	86.91 ± 1.82	88.01 ± 1.78	86.27 ± 1.88	80.29 ± 1.65	93.37 ± 1.55
	3.17 ± 0.03	3.11 ± 0.03	3.12 ± 0.03	2.98 ± 0.03	3.13 ± 0.03	3.22 ± 0.04	2.61 ± 0.03
Lung_CT_nodule	83.22 ± 1.23	84.12 ± 1.38	84.73 ± 1.60	86.34 ± 1.48	83.44 ± 1.32	81.23 ± 1.72	92.11 ± 2.23
	7.87 ± 0.12	6.91 ± 0.09	6.42 ± 0.08	6.19 ± 0.08	7.83 ± 0.11	8.22 ± 0.13	4.89 ± 0.07
LIDC_IDRI	86.77 ± 1.45	87.56 ± 1.33	85.22 ± 1.31	85.79 ± 1.94	87.11 ± 1.72	86.82 ± 2.23	90.81 ± 2.15
	6.87 ± 0.07	6.41 ± 0.07	7.01 ± 0.07	6.95 ± 0.07	6.52 ± 0.07	6.84 ± 0.06	5.98 ± 0.05
COVID19_CT	84.93 ± 1.93	85.99 ± 1.84	86.84 ± 1.59	87.95 ± 1.54	85.59 ± 1.64	84.48 ± 1.78	87.93 ± 1.87
	10.99 ± 0.12	10.13 ± 0.10	9.87 ± 0.09	9.47 ± 0.08	10.48 ± 0.10	11.13 ± 0.12	9.49 ± 0.09
COVID19_3D	65.28 ± 0.82	67.11 ± 0.64	67.43 ± 0.92	68.12 ± 1.17	64.32 ± 0.79	66.91 ± 0.55	67.16 ± 0.82
	23.87 ± 0.43	20.89 ± 0.48	20.13 ± 0.49	19.56 ± 0.36	25.56 ± 0.52	21.44 ± 0.48	20.87 ± 0.42

Lung_nodule_seg, Lung_CT_nodule, LIDC_IDRI), ISD-MAE also performs well, particularly in the Lung_nodule_seg and Lung_CT_nodule datasets, with Dice scores of $93.37 \pm 1.55\%$ and $92.11 \pm 2.23\%$ respectively, also higher than other methods. Looking at the standard deviation, ISD-MAE exhibits relatively small standard deviations across multiple datasets, indicating its performance is relatively stable, less affected by data fluctuations, which is crucial for tasks requiring high-precision predictions like medical image segmentation. The performance of ISD-MAE on 3D images, such as COVID19_CT, while not as high as in 2D images, is still competitive. This also demonstrates the potential and advantages of ISD-MAE in handling complex, multi-dimensional medical imaging data, as well as its strong adaptability.

Noticeably, compared to the performance on pneumonia segmentation tasks, our ISD-MAE pretraining model excelled on the downstream mediastinal tumor segmentation dataset, showing significant improvement. The mediastinal region contains multiple important organs and tissues, often closely adjacent with indistinct boundaries, leading to irregular shapes and blurred edges. ISD-MAE specifically masks intensity and spatial aspects, focusing on local tumor details such as texture and edges at the spatial level. Capturing these local features is particularly crucial for irregularly shaped mediastinal tumors. At the tissue level, considering the overall relationship between the tumor and surrounding tissues and obtaining

contextual information can help determine the tumor’s position and boundaries more accurately. Pneumonia manifestations in chest CT images are relatively straightforward and may not require such a detailed multi-layered masking strategy for effective segmentation, causing ISD-MAE’s advantages to not be fully realized in such scenarios.

In addition to the segmentation results, ISD-MAE also exhibited impressive performance in the downstream classification task, with ROC-AUC scores of 0.94 and 0.91 for COVID19 and GRAM datasets, respectively. This highlights ISD-MAE’s robustness and effectiveness in handling complex medical imaging data and its ability to generalize well across different datasets. Moreover, the high ROC-AUC scores indicate the model’s strong predictive capability and its potential for accurate classification tasks in medical image analysis.

Fig 4 displays our segmentation results. It can be observed that compared to the other 4 methods (CMAE, DAE, CAE, AE), ISD-MAE may more accurately capture the boundaries and details of the lesion area. Particularly, it performs well in segmenting diverse contour areas such as pneumonia (COVID19_2D) and can identify tumors of various shapes and sizes in the Lung_CT_nodule dataset. This suggests that our ISD-MAE has learned more general image features, indicating better generalization ability.

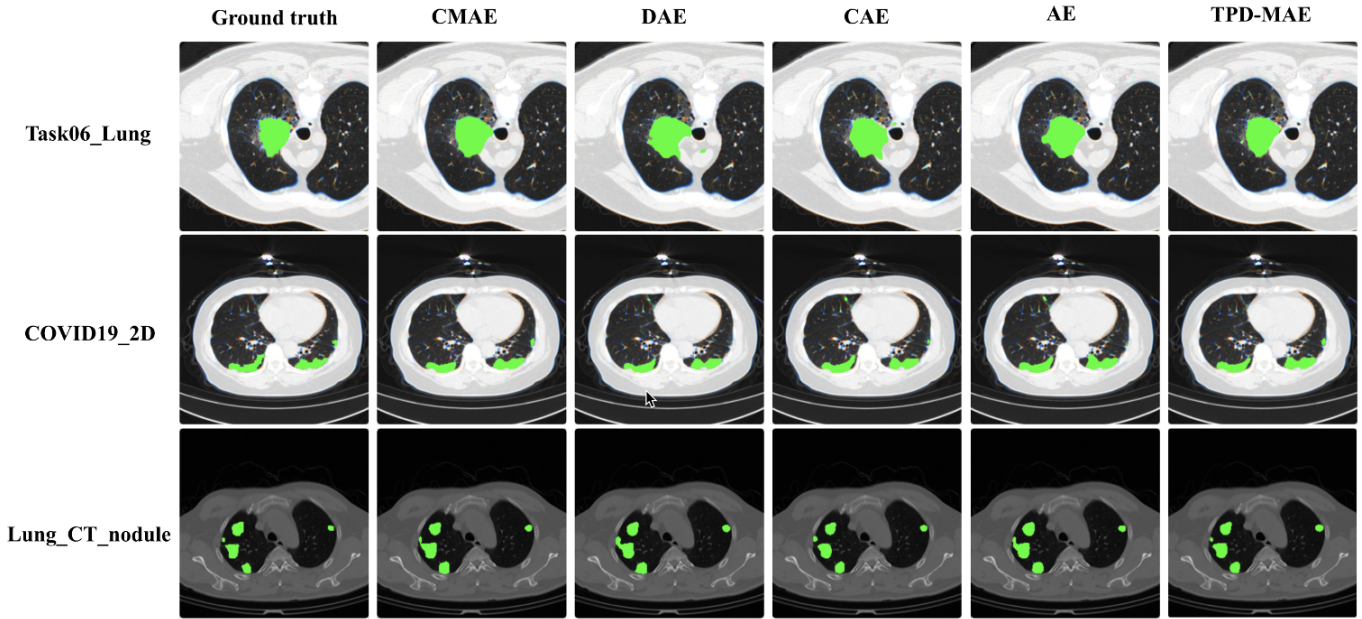


Fig. 4: **Segmentation Result Visualization.** We compared the visualization results on pneumonia and mediastinal tumor datasets for CMAE, DAE, CAE, AE, and our ISD-MAE. It is evident that our ISD-MAE has a clear advantage in delineating the boundary of lesion areas.

B. Performance

a) *DSC scores:* The Fig 5 depicts the online evaluation results of DSC on ISD-MAE, CMAE, and AE for four segmentation tasks. These tasks include pneumonia (COVID19_LESION, COVID19_CT) and mediastinal tumors (Lung_nodule_seg and Lung_CT_nodule), where COVID19_CT is a 3D dataset. From the graph, it can be observed that for the tasks of COVID19_LESION and Lung_nodule_seg, the Dice coefficient of ISD-MAE consistently surpasses CMAE and AE, reaching over 80% DSC almost in the initial stages. For the Lung_CT_nodule dataset, ISD-MAE initially scores lower in the first two epochs but quickly surpasses CMAE and AE thereafter. ISD-MAE may require more time in the initial stages to adapt to the dataset’s characteristics, hence showing suboptimal performance in the first few epochs. However, once the model begins to converge, its performance rapidly improves and surpasses other methods.

However, ISD-MAE does not exhibit significant advantages over the other two methods on the 3D dataset (COVID19_CT). Despite ISD-MAE’s excellent performance on 2D datasets, this does not imply seamless scalability to higher-dimensional datasets. The complexity of 3D datasets is much higher than that of 2D datasets, with 3D images containing more spatial and structural information. The shape and location of tumor or lesion areas may vary more in three-dimensional space, and there is contextual information between adjacent slices that the model needs to effectively capture and utilize. Additionally, 3D image data is massive, requiring substantial computational resources and memory for processing and segmentation. Directly handling the entire 3D image may exceed hardware limitations, necessitating strategies such as segmenting the 3D

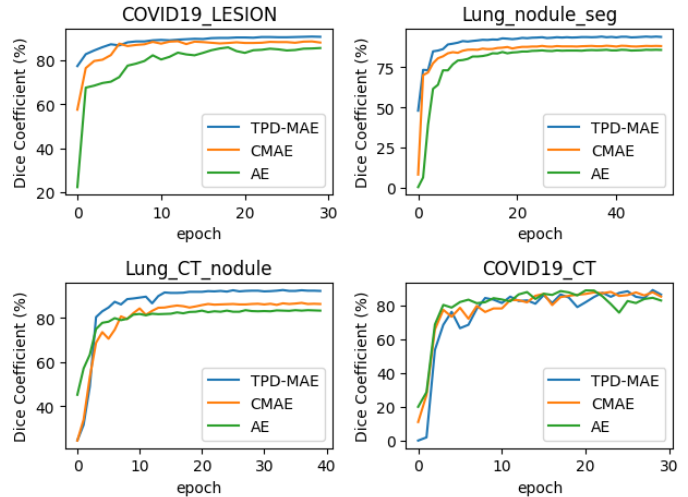


Fig. 5: **The online evaluate of DSC scores for pneumonia and mediastinal tumors.** It can be seen that our ISD-MAE demonstrates significant advantages across multiple tasks, especially in the early stages, quickly achieving optimal results with only a few epochs.

image into sub-volumes for processing, which may lead to some loss of spatial information. The design of ISD-MAE may encounter scalability bottlenecks when dealing with such 3D data, resulting in its performance not significantly surpassing other methods.

b) *Loss:* During the pre-training of images, we plotted the loss function curves (Fig. 6) for the ISD-MAE, CMAE, and AE methods to evaluate their performance during the training process. In the initial stages, the loss function value of ISD-MAE rapidly decreases from a higher level with a

TABLE III: The impact of different masking strategies on downstream segmentation tasks. "Intensity mask only" represents using only intensity masking strategy, while "Spatial mask only" represents using only spatial masking strategy. In each cell of the table, the number above represents the Dice similarity coefficient (%), while the number below represents the Hausdorff distance (HD). The best score in each column is shown in bold.

Strategy \ Datasets	COVID19_LESION	Task06_Lung	COVID19_2D	Lung_nodule_seg	Lung_CT_nodule	LIDC_IDRI	COVID19_CT	COVID19_3D
Intensity mask only	85.02 ± 0.67	87.42 ± 0.89	79.89 ± 1.96	89.45 ± 0.66	84.35 ± 0.46	86.55 ± 0.84	83.68 ± 2.84	67.47 ± 0.60
	22.71 ± 0.19	7.87 ± 0.11	23.09 ± 0.18	4.63 ± 0.13	14.12 ± 0.37	8.02 ± 0.21	14.79 ± 0.77	21.26 ± 0.72
Spatial mask only	85.65 ± 0.45	85.78 ± 0.54	79.12 ± 1.84	90.33 ± 0.78	85.33 ± 0.64	87.05 ± 0.75	82.2 ± 3.42	67.08 ± 0.64
	21.78 ± 0.22	7.41 ± 0.09	23.01 ± 0.19	4.24 ± 0.11	13.85 ± 0.28	8.00 ± 0.17	14.62 ± 0.64	21.39 ± 0.68

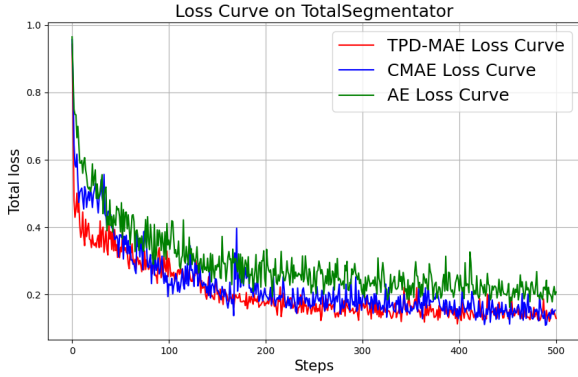


Fig. 6: The loss function curves for pre-trained images on the TotalSegmentator dataset using three different methods (ISD-MAE, CMAE, and AE).

significant magnitude. In comparison, the initial loss function value of CMAE is slightly lower than ISD-MAE, with a relatively slower decrease rate; while AE starts with a higher initial loss function value and a slower decrease rate. As training progresses, the loss function of ISD-MAE continues to steadily decrease, reaching a lower level (approximately 0.1) around 300 steps. The loss function of CMAE also steadily decreases, but its value at 300 steps is still higher than ISD-MAE (approximately 0.18). AE shows an accelerated decrease in this phase, but the overall loss function value remains higher than ISD-MAE and CMAE. In the later stages of training, the loss functions of the three methods tend to stabilize, with CMAE’s final stabilized value slightly higher than ISD-MAE and also higher than AE.

The loss function curves indicate that ISD-MAE exhibits a faster convergence speed and a lower final loss value during pre-training, demonstrating better training performance compared to CMAE and AE.

C. Ablation studies

To evaluate the contributions of intensity masks and spatial masks to model performance, we designed a series of experiments. For instance, while keeping other components constant, we trained the model using only intensity masks or

spatial masks and observed changes in metrics such as Dice coefficient and HD in downstream segmentation tasks.

Table III shows the performance on downstream segmentation tasks after pre-training with different masking strategies. "Intensity mask only" represents using only the intensity masking strategy, while "Spatial mask only" represents using only the spatial masking strategy. From the table, it can be observed that for 2D tasks in pneumonia segmentation, the intensity masking strategy performs better in terms of the Dice coefficient, but the spatial masking strategy excels in the Hausdorff distance (HD), indicating more accurate boundary segmentation. For 3D tasks (COVID19 CT, COVID19 3D), although the difference in Dice coefficients is not significant, the spatial masking strategy still performs better in HD. For the lung nodule dataset, the advantage of the spatial masking strategy is more pronounced, with three lung nodule datasets showing higher Dice coefficients and Hausdorff distances under the spatial masking strategy.

This suggests that the intensity masking strategy performs better in terms of the Dice coefficient, which may imply superior overall segmentation performance, capturing more target areas. The spatial masking strategy excels in the Hausdorff distance (HD), indicating more accurate boundary segmentation results. Therefore, considering a combination of both masking strategies can leverage their respective strengths, making the model more robust and adaptable to different datasets and tasks.

D. Limitation

Although ISD-MAE excels on traditional 2D images, it lacks significant advantages on 3D datasets. The multi-level masking strategy of ISD-MAE may not be flexible or effective enough in 3D space to fully capture the complex features within 3D images. For improvements in this aspect, we believe that work can be expanded in three main areas:

- **Loss functions.** Consider utilizing multi-scale SSIM loss functions and combining them with weighted aggregation for a more comprehensive assessment of structural similarity. Alternatively, integrate DICE loss to simultaneously consider both structural similarity and region overlap in images.

- **Enhanced 3D convolution blocks.** Explore the use of deformable convolutions [24], depthwise separable convolutions [25], etc., which offer better robustness in handling images with scale and rotation changes compared to traditional convolutions, with increased computational efficiency.
- **Datasets:** Process 3D images from multiple perspectives (such as axial, coronal, and sagittal views) and enhance segmentation performance by fusing information from these views. This can be achieved through simple feature concatenation, weighted averaging, or attention mechanisms for integration.

V. CONCLUSION

This paper proposes an improved self-supervised learning method, namely Intensity-Spatial Dual Masked AutoEncoder (ISD-MAE), which introduces a Masked Autoencoder (MAE) branch in the model to perform intensity masking and spatial masking operations on images for multi-scale feature learning and segmentation tasks in chest CT images. By incorporating a dual-branch structure and contrastive learning, the model's ability to learn tissue features and boundary details is enhanced. Experimental results demonstrate that ISD-MAE outperforms other methods significantly in segmentation tasks on 2D pneumonia and mediastinal tumor datasets, but there is still room for improvement in performance on 3D datasets.

ACKNOWLEDGMENT

This work is supported by Computer Architecture Laboratory of Zhejiang University and the Supercomputing Center of Hangzhou City University.

REFERENCES

- [1] Huang, Zhicheng, Xiaojie Jin, Chengze Lu, Qibin Hou, Ming-Ming Cheng, Dongmei Fu, Xiaohui Shen, and Jiashi Feng. "Contrastive masked autoencoders are stronger vision learners." *IEEE Transactions on Pattern Analysis and Machine Intelligence* (2023).
- [2] Bao, Hangbo, Li Dong, Songhao Piao, and Furu Wei. "Beit: Bert pre-training of image transformers." *arXiv preprint arXiv:2106.08254* (2021).
- [3] He, Kaiming, Xinlei Chen, Saining Xie, Yanghao Li, Piotr Dollár, and Ross Girshick. "Masked autoencoders are scalable vision learners." In *Proceedings of the IEEE/CVF conference on computer vision and pattern recognition*, pp. 16000-16009. 2022.
- [4] Zheng, Jie, Ru Wen, Haiqin Hu, Lina Wei, Kui Su, Wei Chen, Chen Liu, and Jun Wang. "Tissue-Contrastive Semi-Masked Autoencoders for Segmentation Pretraining on Chest CT." *arXiv preprint arXiv:2407.08961* (2024).
- [5] Ronneberger, Olaf, Philipp Fischer, and Thomas Brox. "U-net: Convolutional networks for biomedical image segmentation." In *Medical image computing and computer-assisted intervention—MICCAI 2015: 18th international conference, Munich, Germany, October 5-9, 2015, proceedings, part III 18*, pp. 234-241. Springer International Publishing, 2015.
- [6] Çiçek, Özgün, Ahmed Abdulkadir, Soeren S. Lienkamp, Thomas Brox, and Olaf Ronneberger. "3D U-Net: learning dense volumetric segmentation from sparse annotation." In *Medical Image Computing and Computer-Assisted Intervention—MICCAI 2016: 19th International Conference, Athens, Greece, October 17-21, 2016, Proceedings, Part II 19*, pp. 424-432. Springer International Publishing, 2016.

- [7] Zhou, Zongwei, Md Mahfuzur Rahman Siddiquee, Nima Tajbakhsh, and Jianming Liang. "Unet++: A nested u-net architecture for medical image segmentation." In *Deep Learning in Medical Image Analysis and Multimodal Learning for Clinical Decision Support: 4th International Workshop, DLMIA 2018, and 8th International Workshop, ML-CDS 2018, Held in Conjunction with MICCAI 2018, Granada, Spain, September 20, 2018, Proceedings 4*, pp. 3-11. Springer International Publishing, 2018.
- [8] Hinton, Geoffrey E., and Ruslan R. Salakhutdinov. "Reducing the dimensionality of data with neural networks." *science* 313, no. 5786 (2006): 504-507.
- [9] Vincent, Pascal, Hugo Larochelle, Yoshua Bengio, and Pierre-Antoine Manzagol. "Extracting and composing robust features with denoising autoencoders." In *Proceedings of the 25th international conference on Machine learning*, pp. 1096-1103. 2008.
- [10] Kingma, Diederik P. "Auto-encoding variational bayes." *arXiv preprint arXiv:1312.6114* (2013).
- [11] Chen, Ting, Simon Kornblith, Mohammad Norouzi, and Geoffrey Hinton. "A simple framework for contrastive learning of visual representations." In *International conference on machine learning*, pp. 1597-1607. PMLR, 2020.
- [12] He, Kaiming, Haoqi Fan, Yuxin Wu, Saining Xie, and Ross Girshick. "Momentum contrast for unsupervised visual representation learning." In *Proceedings of the IEEE/CVF conference on computer vision and pattern recognition*, pp. 9729-9738. 2020.
- [13] Grill, Jean-Bastien, Florian Strub, Florent Althé, Corentin Tallec, Pierre Richemond, Elena Buchatskaya, Carl Doersch et al. "Bootstrap your own latent—a new approach to self-supervised learning." *Advances in neural information processing systems* 33 (2020): 21271-21284.
- [14] Caron, Mathilde, Hugo Touvron, Ishan Misra, Hervé Jégou, Julien Mairal, Piotr Bojanowski, and Armand Joulin. "Emerging properties in self-supervised vision transformers." In *Proceedings of the IEEE/CVF international conference on computer vision*, pp. 9650-9660. 2021.
- [15] Chaitanya, Krishna, Ertunc Erdil, Neerav Karani, and Ender Konukoglu. "Contrastive learning of global and local features for medical image segmentation with limited annotations." *Advances in neural information processing systems* 33 (2020): 12546-12558.
- [16] Chen, Min, Xiaobo Shi, Yin Zhang, Di Wu, and Mohsen Guizani. "Deep feature learning for medical image analysis with convolutional autoencoder neural network." *IEEE Transactions on Big Data* 7, no. 4 (2017): 750-758.
- [17] Xie, Enze, Wenhai Wang, Zhiding Yu, Anima Anandkumar, Jose M. Alvarez, and Ping Luo. "SegFormer: Simple and efficient design for semantic segmentation with transformers." *Advances in neural information processing systems* 34 (2021): 12077-12090.
- [18] Wang, Zhou, Alan C. Bovik, Hamid R. Sheikh, and Eero P. Simoncelli. "Image quality assessment: from error visibility to structural similarity." *IEEE transactions on image processing* 13, no. 4 (2004): 600-612.
- [19] Wasserthal, Jakob, Hanns-Christian Breit, Manfred T. Meyer, Maurice Pradella, Daniel Hinck, Alexander W. Sauter, Tobias Heye et al. "TotalSegmentator: robust segmentation of 104 anatomic structures in CT images." *Radiology: Artificial Intelligence* 5, no. 5 (2023).
- [20] Rumelhart, David E., Geoffrey E. Hinton, and Ronald J. Williams. "Learning representations by back-propagating errors." *nature* 323, no. 6088 (1986): 533-536.
- [21] Vincent, Pascal, Hugo Larochelle, Yoshua Bengio, and Pierre-Antoine Manzagol. "Extracting and composing robust features with denoising autoencoders." In *Proceedings of the 25th international conference on Machine learning*, pp. 1096-1103. 2008.
- [22] Chen, Xiaokang, Mingyu Ding, Xiaodi Wang, Ying Xin, Shentong Mo, Yunhao Wang, Shumin Han, Ping Luo, Gang Zeng, and Jingdong Wang. "Context autoencoder for self-supervised representation learning." *International Journal of Computer Vision* 132, no. 1 (2024): 208-223.
- [23] Wei, Chen, Haoqi Fan, Saining Xie, Chao-Yuan Wu, Alan Yuille, and Christoph Feichtenhofer. "Masked feature prediction for self-supervised visual pre-training." In *Proceedings of the IEEE/CVF Conference on Computer Vision and Pattern Recognition*, pp. 14668-14678. 2022.
- [24] Dai, Jifeng, Haozhi Qi, Yuwen Xiong, Yi Li, Guodong Zhang, Han Hu, and Yichen Wei. "Deformable convolutional networks." In *Proceedings of the IEEE international conference on computer vision*, pp. 764-773. 2017.
- [25] Chollet, François. "Xception: Deep learning with depthwise separable convolutions." In *Proceedings of the IEEE conference on computer vision and pattern recognition*, pp. 1251-1258. 2017.